



Full length article

Electrochemical potential in multilayer solid electrolytes and mechanical implications

So Yeon Kim ^a, Ju Li ^{a,b},*^a Department of Nuclear Science and Engineering, Massachusetts Institute of Technology, 77 Massachusetts avenue, Cambridge, 02139, MA, United States^b Department of Materials Science and Engineering, Massachusetts Institute of Technology, 77 Massachusetts avenue, Cambridge, 02139, MA, United States

ARTICLE INFO

Keywords:

All-solid-state batteries
Solid electrolytes
Electrochemo-mechanical degradation
Multilayer
Theory and simulations

ABSTRACT

Rechargeable all-solid-state batteries (ASSBs) offer improved safety and the potential for advanced chemistries, but the susceptibility of solid electrolytes (SEs) to electrochemo-mechanical degradation remains a major challenge. This degradation manifests in two modes: a fast longitudinal mode, such as short-circuiting dendrites, and a slow transverse mode, such as in-plane cracking and isolated alkali metal formation. While prior research has mainly focused on mitigating the longitudinal mode, the transverse mode is becoming increasingly critical, particularly under the practically required pressure-less conditions. Here, we demonstrate through thermodynamic modeling that multilayering the SE separator can mitigate electrochemical instabilities attributed to abrupt jumps in the chemical potential of neutral Li atoms (Li^0) within the SE separator, contributing to transverse mechanical degradation. We first derive an analytic solution for the Li^0 chemical potential profile within SEs, confirming its extreme sensitivity to SE-specific redox-sensitive electronic conductivities and boundary potentials at the SE edges. Inspired by this sensitivity, we propose and theoretically demonstrate that multilayering can confine potential jumps to less detrimental spatial/ Li^0 -potential regimes, thereby mitigating transverse degradation and delaying longitudinal degradation as well. We then discuss the effects of both extrinsic and intrinsic factors on this approach, along with their practical implications. Overall, our findings suggest that multilayered SEs can provide a comprehensive strategy against both transverse and longitudinal degradation modes, outlining critical parameters to consider in the development of pressure-less ASSBs with enhanced electrochemical performance and damage resistance.

1. Introduction

Rechargeable all-solid-state batteries (ASSBs) hold promise for reducing fire hazards and enabling advanced battery chemistries [1]. Achieving the practical feasibility of ASSBs requires mitigating the electrochemo-mechanical degradation of ceramic solid electrolyte (SE) separators [2,3]. These ceramic SEs typically have limited capacity to relieve mechanical stress [4,5] and are often not chemically stable against body-centered cubic alkali metals like Li_{BCC} [6,7]. The repetitive plating and stripping of Li_{BCC} thus often induce electrochemo-mechanical instabilities, such as longitudinal or transverse SE cracks [3, 8]. These instabilities can lead to the loss of cyclable Li, increased charge-transfer resistance, short-circuiting, etc., especially under abusive cycling conditions such as high charging/discharging rates, no externally applied pressures, and/or no initial Li_{BCC} anodes. In terms of battery performance, these phenomena can result in low energy density, poor cycle life, and reduced device reliability, delaying ASSBs' commercial viability.

Microscopically, degradation mechanisms in ASSBs can be broadly classified into two categories [8]. The first is the fast longitudinal mode, which accumulates degradation parallel to the ionic current, such as short-circuiting dendrite formation. Its origin has long been debated, but recent studies suggest that this mode initially arises from a combination of current focusing and pre-existing nanoscale subsurface pores and cracks, rather than from electronic leakage or electrochemical reduction [4,5]. Specifically, these studies link crack initiation to Li_{Metal} (not necessarily in the BCC phase) deposition into subsurface pores via microcracks that connect to the surface [4,5]. As charging continues, pressure builds in the pores due to the slow extrusion of Li_{Metal} back to the surface via plastic flow, leading to crack formation [4]. Additionally, the propagation of initiated cracks was attributed to wedge opening, where Li_{Metal} pushes the crack from the rear rather than the tip [4]. This degradation model was corroborated by observations that reducing stack pressure extends cycle life before

* Corresponding author.

E-mail address: liju@mit.edu (J. Li).<https://doi.org/10.1016/j.actamat.2025.120982>

Received 8 December 2024; Received in revised form 20 February 2025; Accepted 24 March 2025

Available online 1 April 2025

1359-6454/© 2025 Acta Materialia Inc. Published by Elsevier Inc. All rights are reserved, including those for text and data mining, AI training, and similar technologies.

short-circuiting [4], and that densifying SE separators increases the critical current density [9].

The second category is the slow transverse mode, which accumulates damage perpendicular to the ionic current, manifesting as bowl-shaped or in-plane cracking and the evolution of isolated alkali metal islands (disconnected from the surface). This mode has been attributed to electronic and ionic transport bottlenecks within the SEs [10]. An ion conductor features a generic electronic bottleneck, where the sum of electron and hole conductivities ($\sigma_{e^-} + \sigma_{h^+}$) drops sharply, causing the heterogeneous distribution of marginal $\text{Li}^0(\text{SE})$ [11]. Large variations in equilibrium lattice constant across this narrow transition zone between highly reduced and highly oxidized SEs can generate significant eigen-strain mismatch, leading to brittle fracture resembling a shock front [10]. Furthermore, abrupt electronic bottlenecks make SE separators particularly vulnerable to Li^0 chemical potential overshoots or undershoots at ionic bottlenecks, such as grain boundaries, which can induce oxygen evolution or alkali metal island formation within the SE [11,12]. Notably, a recent *in situ* magnetic resonance imaging study revealed that subsurface Li_{Metal} deposition is followed by the formation of isolated Li_{Metal} due to electrolyte reduction in deeper regions of the SE, along with a subsequent interaction between crack/dendrite propagation and continued SE reduction [13]. This finding suggests an interplay between two modes of degradation.

Most research has focused on addressing longitudinal degradation. Mitigation strategies typically involve an additional layer [14], ranging from mixed ionic-electronic conductors (MIECs) with high electronic transference numbers (t_e) [15] to those with $t_e \sim 0$, which essentially act as SEs [16]. From a damage control perspective, the former typically aims to delay damage initiation, while the latter often focuses on resisting propagation. For example, by varying the ionic and electronic conductivities and lithiophilicity of a mixed conducting layer, Li_{BCC} plating/stripping can be directed away from the SE separators, preventing electrochemo-mechanical instabilities [17]. On the other hand, multilayering of SE separators can inhibit dendrite crack propagation, especially when the SE layer near the cathode decomposes upon contact with Li_{Metal} , accompanied by volume expansion, which blocks further Li_{Metal} penetration through an expansion-screw effect [16]. Furthermore, X-ray tomographic imaging of multilayered SE separators has recently revealed two additional crack resistance mechanisms: crack deflection along mechanically weak interfaces due to local mismatches in elastic moduli, and lateral crack deflection within a sandwiched SE containing preferentially oriented particles [18].

The transverse mode has received less emphasis but is becoming increasingly important with the pursuit of pressure-less capability for practical feasibility. Without externally applied stack pressure, this degradation mode is expected to initiate more easily due to its sensitivity to conformal contact between SEs and electrodes, potentially leading to complete electrical disconnection once initiated. This calls for mitigation strategies that are effective for both modes of degradation, naturally raising the question of whether current strategies for mitigating longitudinal degradation can also be effective for the transverse mode.

In this context, we demonstrate through thermodynamic modeling that multilayering can effectively reduce the SE separators' susceptibility to both modes of degradation. We first derive an analytic solution for the Li^0 chemical potential within SE separators and confirm its sensitivity to boundary potentials. Motivated by this sensitivity, we show that potential jumps induced by the generic electronic bottlenecks can be confined to the separator's edges when the separator is composed of multilayers of SEs, each exhibiting such bottlenecks at different Li^0 chemical potentials; at the edges, local stress caused by lattice mismatch is less detrimental, as it can be relieved along the surface. This confinement also prevents potential jumps due to ionic bottlenecks from causing Li^0 chemical potential overshoots/undershoots, thereby mitigating detrimental Li_{Metal} formation within the SE separator. Ultimately, this strategy mitigates both transverse degradation and

transverse instability-assisted longitudinal degradation. Additionally, since SE multilayering is also pursued for high-voltage cathodes, these results suggest that multilayering SE separators could potentially serve as an all-in-one strategy for the electrochemo-mechanical stability of SE separators.

2. Theory

2.1. Transport-induced potential jumps and mechanical degradation

As briefly discussed in the Introduction, transverse degradation refers to the accumulation of damage perpendicular to the ionic current. Historically, it has been more extensively studied in solid oxide fuel/electrolysis cells. Examples include electrolyte cracking that propagates in-plane rather than through the thickness, as well as oxygen bubble evolution occurring primarily at transverse grain boundaries, giving the appearance of in-plane extension (Fig. 1a). More recently, this discussion has expanded to solid-state batteries, following the observation of bowl-shaped cracking—partially involving in-plane cracking similar to that seen in solid oxide electrolysis cells—near Li metal anodes that precede the well-known longitudinal cracking, which propagates along the ionic current and is directly associated with final battery failure (Fig. 1b).

This degradation mode has been attributed to transport bottlenecks, which refer to regions where the conductivity of charge carriers is several orders of magnitude lower than in most other areas of the SEs [10]. Such bottlenecks can arise in both ionic and electronic transport pathways. In yttrium-stabilized zirconia (YSZ), a fast oxygen-ion conductor used in solid oxide electrolysis cells, grain boundaries serve as bottlenecks in the ionic channel, exhibiting O^{2-} conductivity that is several orders of magnitude lower than in the bulk lattice [11]. In the electronic channel, transport bottlenecks may result from compositional or structural inhomogeneities. However, the most fundamental bottleneck is a universal one, occurring at the point where the sum of electron and hole conductivities reaches a minimum. Since conductivity is proportional to the concentration of charge carriers, and electron and hole concentrations exhibit an exponential dependence on the chemical potential of the species of interest, electron and hole conductivities are highly nonlinear and can vary by several orders of magnitude. For example, in YSZ, electronic conductivity can fluctuate by 4–5 orders of magnitude even at high temperatures exceeding 1273 K [20]. Due to their temperature dependence, this variation becomes even more pronounced at lower temperatures, making electronic conductivities even more nonlinear at ambient temperatures relevant to solid-state batteries.

These transport bottlenecks in ion or electron flow within SEs can cause sharp jumps in the chemical potential of the neutral form of the relevant chemical species (e.g., Li^0 or O_2). Here, we first provide a physical picture qualitatively, following the well-documented description in Ref. [11]. In a nominally “good” SE, the fastest ion species (e.g., Li^+ in Li-ion conductors or O^{2-} in oxygen-ion conductors) has a little chemical potential gradient, meaning its movement is driven mostly by the electrostatic potential gradient (Fig. S1). In contrast, the electronic disorder can experience a strong gradient in chemical potential as well as a gentle gradient in electrostatic potential. We discuss two scenarios: (1) electronic bottleneck and (2) ionic bottleneck. First, assuming it is not an internal crack, an electronic bottleneck does not necessarily coincide with an ionic bottleneck. At a steady state, the ion flow must remain constant, meaning there is no jump in the electrostatic potential at the electronic bottleneck. However, to maintain a steady electronic flow across the electronic bottleneck, a jump in the electron chemical potential is required, leading to a steep electron electrochemical potential gradient (i.e., a strong driving force for electron transport). Second, at an ionic bottleneck, a jump in electrostatic potential is necessary, as it serves as the primary driving force for maintaining a constant ion flow. Meanwhile, assuming a constant electronic flow—since an ionic

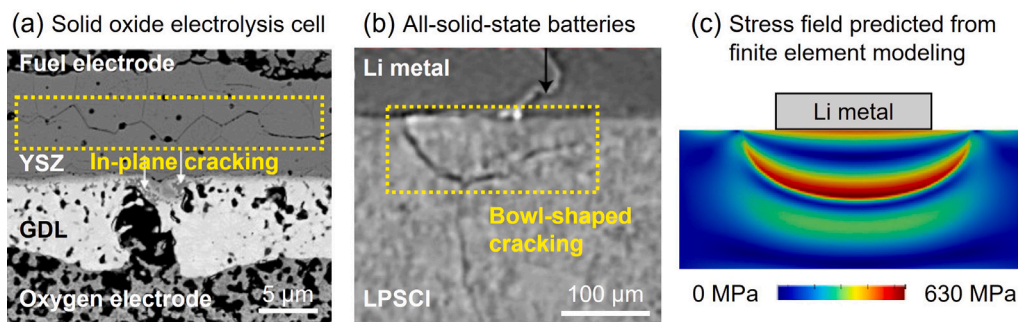


Fig. 1. Transverse degradation of solid electrolytes. (a) In-plane cracking in yttrium-stabilized zirconia (YSZ) in a solid oxide electrolysis cell. GDG: gas diffusion layer. Reproduced with permission from Ref. [19]. Copyright 2021 Elsevier Ltd. (b) Bowl-shaped cracking in argyrodite (LPSCI) in an all-solid-state battery. Reproduced with permission from Ref. [3]. Copyright 2021 Springer Nature. (c) von Mises stress field predicted by finite element modeling, showing a bowl-shaped region with high stress reaching several hundred MPa. Reproduced with permission from Ref. [10]. Copyright 2024 Elsevier Ltd.

bottleneck does not inherently coincide with an electronic bottleneck—the electron electrochemical potential should remain linear, without a jump at the ionic bottleneck. Consequently, any jump in electrostatic potential must be counterbalanced by a corresponding jump in the electron chemical potential. In the meantime, variations in electron chemical potential lead to corresponding variations in the chemical potential of Li^0 or O_2 , assuming local equilibrium of the redox reactions, as will be quantitatively analyzed in the subsequent sections. Hence, a potential jump occurs at every transport bottleneck, regardless of whether it is in the ionic or electronic channel.

Furthermore, atomic rearrangement driven by such potential jumps induces significant mechanical stress (Fig. 1c). First, a generic electronic bottleneck can cause potential jumps as large as several electron volts (eV), leading to a heterogeneous distribution of marginal $\text{Li}^0(\text{SE})$. It is important to note that $\text{Li}^0(\text{SE})$ does not represent a metallic lithium atom exsolved from the SE lattice. It can instead be considered a composite particle in which Li^0 is bound to an excess electron within the atomic structure of the SE. A detailed description of this hypothetical immobile particle can be found in Ref. [10]. Since excess $\text{Li}^0(\text{SE})$ storage leads to local volume expansion, the resulting stress distribution in SEs can be analyzed using the eigen-strain method. Finite element modeling [10] has shown that the von Mises stress field at potential jumps caused by an electronic bottleneck can reach several hundred MPa (Fig. 1c), which can, in fact, induce brittle fracture in SEs. This provides a possible explanation for the bowl-shaped cracking observed in experiments (Fig. 1b). Moreover, ionic bottlenecks in SEs near electrodes can generate potential jumps large enough to push the chemical potential of a charge-neutral species beyond its boundary values at the two electrodes, a phenomenon known as “overshoot” or “undershoot” [11]. Such a phenomenon can trigger the formation of unexpected neutral phases, such as gaseous O_2 or solid alkali metal phases, within the SE [11]. These phases typically lead to stress accumulation, structural distortions, fractures, and short circuits, ultimately contributing to device deterioration and failure [3,21].

It should also be noted that the resulting degradation can be synergistic and self-reinforcing. The large potential jump at a generic electronic bottleneck makes the edges of SEs near the electrodes particularly vulnerable to overshoots or undershoots. While potential jumps at ionic bottlenecks are typically less than 1 eV, if they develop within the SE near the electrode—where the potential is already close to that of the electrode—smaller jumps may still be sufficient to push the local Li^0 chemical potential beyond the boundary potentials, leading to the precipitation of neutral phases such as Li metal islands or oxygen bubbles. Once neutral phases precipitate, they not only introduce internal stress but can also locally amplify stress generated by other sources, leading to crack nucleation and facilitating crack propagation. The transverse portion of propagating cracks inherently acts as a transport bottleneck, causing further potential jumps and exacerbating degradation. Moreover, when internal cracks connect with the electrodes,

longitudinal crack propagation can be enhanced by wedge-opening mechanisms. As a result, regions susceptible to overshoots or undershoots would extend as neutral phases within the SE, now in contact with the electrodes, effectively reset the SE-electrode boundary, shifting it further into the SE. In other words, transverse and longitudinal degradation modes positively reinforce each other, working synergistically to accelerate bulk electrochemo-mechanical degradation, which manifests as cracking and ultimately leads to increased impedance and short-circuiting. Therefore, engineering the electrochemical potential profiles within SE separators—e.g., minimizing the magnitude of potential jumps or strategically tailoring their positions so that jumps of a given magnitude are less detrimental—is critically important for mitigating mechanical degradation and preventing battery failure.

2.2. Mathematical formulation of electrochemical potential inside solid electrolytes

As briefly discussed in Section 2.1, the Li^0 chemical potential profile inside SE separators is correlated with the transport bottlenecks of charged species, despite Li^0 being a neutral species not expected to permeate through the SE separators. This correlation arises from a redox reaction involving both Li^0 and charged species, as well as the dependence of charge fluxes on chemical and electrostatic potentials. To derive a closed-form solution for the Li^0 chemical potential profile inside SE separators, we assume a hypothetical Li conductor with mixed ionic and electronic conductions and focus on a one-dimensional (1D) problem along the x -direction. Assumptions similar to those made in Ref. [20] for the numerical modeling of oxygen conductors in solid oxide fuel/electrolysis cells are adopted. Specifically, we consider only the motion of Li^+ ions and electrons, given the limited mobilities of other species (e.g., La^{3+} , Zr^{4+} , and O^{2-} in $\text{Li}_7\text{La}_3\text{Zr}_2\text{O}_{12}$ (LLZO)) at room temperature. We also assume local equilibrium for the following two reactions:



These two reversible reactions in dynamic equilibrium correspond to the following electrochemical potential equilibria:

$$\tilde{\mu}_{\text{Li}^+} + \tilde{\mu}_{\text{e}^-} = \tilde{\mu}_{\text{Li}^0} = \mu_{\text{Li}^0} \quad (3)$$

$$\tilde{\mu}_{\text{e}^-} + \tilde{\mu}_{\text{h}^+} = 0 \quad (4)$$

Li^0 is charge-neutral, meaning its electrochemical potential ($\tilde{\mu}_{\text{Li}^0}$) is essentially the same as its chemical potential (μ_{Li^0}). Therefore, μ_{Li^0} will be referred to as the “ Li^0 potential” for brevity hereafter unless further clarification is needed.

The charged species can generate both drift currents driven by external electrostatic fields and diffusion currents driven by chemical potential gradients [22]. We combine these terms to express the current density (j_{R^n}) for each charged species (R^n , where n denotes the net charge of the species) in terms of its electrochemical potential ($\tilde{\mu}_{R^n}$) and conductivity (σ_{R^n}), with the electron charge denoted as e , as follows:

$$j_{\text{Li}^+} = -\frac{\sigma_{\text{Li}^+}}{e} \frac{d\tilde{\mu}_{\text{Li}^+}}{dx} \quad (5)$$

$$j_{e^-} = \frac{\sigma_{e^-}}{e} \frac{d\tilde{\mu}_{e^-}}{dx} \quad (6)$$

$$j_{\text{h}^+} = \frac{\sigma_{\text{h}^+}}{e} \frac{d\tilde{\mu}_{e^-}}{dx} \quad (7)$$

The total current density (j_{total}) is the sum of these components:

$$j_{\text{total}} = j_{\text{Li}^+} + j_{e^-} + j_{\text{h}^+} = -\frac{\sigma_{\text{Li}^+}}{e} \frac{d\tilde{\mu}_{\text{Li}^+}}{dx} + \frac{\sigma_{e^-} + \sigma_{\text{h}^+}}{e} \frac{d\tilde{\mu}_{e^-}}{dx} \quad (8)$$

The Li^+ flow is then related to the Li mass flow (J_{Li}) as follows:

$$J_{\text{Li}} = \frac{j_{\text{Li}^+}}{e} = -\frac{\sigma_{\text{Li}^+}}{e^2} \frac{d\tilde{\mu}_{\text{Li}^+}}{dx} \quad (9)$$

The above equations can be expressed in matrix form:

$$\begin{bmatrix} -e^2 J_{\text{Li}} \\ e j_{\text{total}} \end{bmatrix} = \begin{bmatrix} \sigma_{\text{Li}^+} & 0 \\ -\sigma_{\text{Li}^+} & \sigma_{e^-} + \sigma_{\text{h}^+} \end{bmatrix} \begin{bmatrix} \frac{d\tilde{\mu}_{\text{Li}^+}}{dx} \\ \frac{d\tilde{\mu}_{e^-}}{dx} \end{bmatrix} \quad (10)$$

which can be rewritten as:

$$\begin{bmatrix} \frac{d\tilde{\mu}_{\text{Li}^+}}{dx} \\ \frac{d\tilde{\mu}_{e^-}}{dx} \end{bmatrix} = \frac{1}{\Delta} \begin{bmatrix} \sigma_{e^-} + \sigma_{\text{h}^+} & 0 \\ \sigma_{\text{Li}^+} & \sigma_{\text{Li}^+} \end{bmatrix} \begin{bmatrix} -e^2 J_{\text{Li}} \\ e j_{\text{total}} \end{bmatrix} \quad (11)$$

where the determinant $\Delta = \sigma_{\text{Li}^+}(\sigma_{e^-} + \sigma_{\text{h}^+})$.

Using Eq. (3), we can express $\frac{d\mu_{\text{Li}^0}}{dx}$ as:

$$\begin{aligned} \frac{d\mu_{\text{Li}^0}}{dx} &= \frac{d\tilde{\mu}_{\text{Li}^+}}{dx} + \frac{d\tilde{\mu}_{e^-}}{dx} \\ &= \frac{1}{\Delta} [(\sigma_{e^-} + \sigma_{\text{h}^+})(-e^2 J_{\text{Li}}) + \sigma_{\text{Li}^+}(-e^2 J_{\text{Li}} + e j_{\text{total}})] \\ &= e j_{\text{total}} \left[\frac{1}{\sigma_{\text{Li}^+}} \left(-\frac{e J_{\text{Li}}}{j_{\text{total}}} \right) + \frac{1}{\sigma_{e^-} + \sigma_{\text{h}^+}} \left(-\frac{e J_{\text{Li}}}{j_{\text{total}}} + 1 \right) \right] \end{aligned} \quad (12)$$

At steady state, $t_{\text{Li}} = \frac{e J_{\text{Li}}}{j_{\text{total}}}$ is a constant of x , as are J_{Li} and j_{total} , or otherwise Li^0 concentration would change with time (Faradaic reaction) in this 1D SE. The dimensionless t_{Li} is always positive, since J_{Li} and j_{total} share the same sign. Eq. (12) can thus be rewritten with t_{Li} and the thickness of the hypothetical Li conductor (L) as:

$$\frac{d\mu_{\text{Li}^0}}{d\left(\frac{x}{L}\right)} = e L j_{\text{total}} \left(\frac{-t_{\text{Li}}}{\sigma_{\text{Li}^+}} + \frac{1-t_{\text{Li}}}{\sigma_{e^-} + \sigma_{\text{h}^+}} \right) \quad (13)$$

In a nominally “good” SE, the Li-ion concentration is nearly constant, as measured experimentally. Thus, σ_{Li^+} can be considered nearly constant, independent of μ_{Li^0} , because the mobility of individual Li^+ does not really care about whether the SE is “oxidized” (slightly Li^0 deficient, $\delta(x) < 0$) or “reduced” (slightly Li^0 excess, $\delta(x) > 0$), as long as no phase transition has been triggered, e.g., within the electrochemical stability window of the SE. This does not mean the total Li concentration in say, $\text{Li}_{7+\delta(x)}\text{La}_3\text{Zr}_2\text{O}_{12}$, is truly a constant across the SE, as the SE could exchange Li with contacting electrodes; it is just that $\delta(x)$ is typically much smaller than 1. However, even small $\delta(x)$ can cause drastic changes in μ_{e^-} and σ_{e^-} , as demonstrated by dopants at the parts-per-billion (ppb) level in silicon. The electronic conductivity ($\sigma_{e^-} + \sigma_{\text{h}^+}$) may thus vary significantly due to changes in electron and hole concentrations according to local redox conditions. Under the dilute limit, these conductivities can be expressed in terms of μ_{Li^0} , based on standard defect chemistry [22]:

$$\sigma_{e^-} = A \exp\left(-\frac{\mu_{\text{Li}^0} - B}{k_{\text{B}}T}\right) \quad (14)$$

$$\sigma_{\text{h}^+} = A \exp\left(\frac{\mu_{\text{Li}^0} - B}{k_{\text{B}}T}\right) \quad (15)$$

where A and B are SE-specific constants.

We can then rearrange Eq. (13) and obtain an indefinite integral, $F(\mu_{\text{Li}^0})$, as follows:

$$\int d\left(\frac{x}{L}\right) = \frac{1}{e L j_{\text{total}}} \int \frac{d\mu_{\text{Li}^0}}{\left(\frac{-t_{\text{Li}}}{\sigma_{\text{Li}^+}} + \frac{1-t_{\text{Li}}}{\sigma_{e^-} + \sigma_{\text{h}^+}}\right)} = F(\mu_{\text{Li}^0}) \quad (16)$$

$$F(\mu_{\text{Li}^0}) = \frac{2A k_{\text{B}}T}{(1-t_{\text{Li}})e L j_{\text{total}}} \left(\frac{\mu_{\text{Li}^0} - B}{a k_{\text{B}}T} - \frac{2 \arctan\left(\frac{(-1+a) \tanh\left(\frac{\mu_{\text{Li}^0} - B}{2k_{\text{B}}T}\right)}{\sqrt{-1+a^2}}\right)}{a \sqrt{-1+a^2}} \right) + C \quad (17)$$

Here, $a = \frac{2A t_{\text{Li}}}{\sigma_{\text{Li}^+}(\mu_{\text{Li}^0} - 1)}$, and C is the constant of integration. The derivation of the analytical solution for the relationship between a normalized position (x/L) and μ_{Li^0} in implicit form is now complete. Below, we simulate μ_{Li^0} profile, assuming specific values for A and B , L , T , and j_{total} in Eq. (17). Then, C and t_{Li} are the two unknowns to be determined by the boundary conditions. First, C will be set to adjust the x/L values to range from 0 to 1. In other words, its value depends on the choice of spatial reference (i.e., the point at which $x = 0$ in the 1D SE layer). As this constant arises due to an arbitrary reference shift, it does not have an intrinsic physical meaning, although it ensures mathematical consistency with the boundary conditions. Second, t_{Li} may differ depending on specific scenarios. This is because the expression for t_{Li} can be rewritten as follows: $t_{\text{Li}} = j_{\text{Li}^+}/j_{\text{total}} = (j_{\text{total}} - j_{e^-} - j_{\text{h}^+})/j_{\text{total}}$; while j_{total} is assumed to be constant throughout this work, the steady-state values of ($j_{e^-} + j_{\text{h}^+}$) can vary depending on the boundary potentials and the presence of transport bottlenecks, thereby affecting t_{Li} .

3. Results

3.1. Extreme sensitivity of potential jump position on boundary potentials

Fig. 2 shows the distributions of μ_{Li^0} in single-layer SE separators with no ionic bottleneck under different applied boundary potentials as a function of x/L —obtained by calculating $F(\mu_{\text{Li}^0})$ using Eq. (17)—along with the conductivity diagram used for calculations. The SE was assumed to be LLZO, a representative oxide SE. The σ_{Li^+} of LLZO is assumed to be redox-insensitive (to within a certain μ_{Li^0} window), while its σ_{e^-} and σ_{h^+} are redox-sensitive, as shown in Fig. 2a. The physical reason for this key underlying assumption is that electronic disorders are the minority disorders in LLZO and in reality should exist as mobile polarons centered on La, Zr, O, whereas the majority, ionic disorder is the mobile Li^+ . Like doped silicon, we know a small amount of off-stoichiometry $\delta(x)$ in $\text{Li}_{7+\delta(x)}\text{La}_3\text{Zr}_2\text{O}_{12}$ can drastically change μ_{e^-} and the polaron concentrations; changing the sign of $\delta(x)$ can even turn it from p-doped to n-doped. Nonetheless, unlike silicon, when well confined within the Brouwer triangle region in Fig. 2a, the polaron concentrations are still much smaller than the mobile Li^+ concentration, and do not affect the physical mobility of Li^+ very much. Given the nearly constant concentration and constant mobility of Li^+ , we can therefore approximate σ_{Li^+} to be nearly independent of μ_{Li^0} , while $\sigma_{e^-}/\sigma_{\text{h}^+}$ are varying wildly.

The kinetic situation becomes more interesting when coming to the edges of the triangular window in Fig. 2a (if we are plotting the concentrations of disorders as standard Brouwer diagrams do), where the polaron concentration starts to match the Li^+ concentration. Strong entanglements between mobile polarons and mobile Li^+ (often imagined to be on a molten sublattice) may occur in this mixed conductor [23], affecting the mobility of Li^+ and thus σ_{Li^+} . This is when

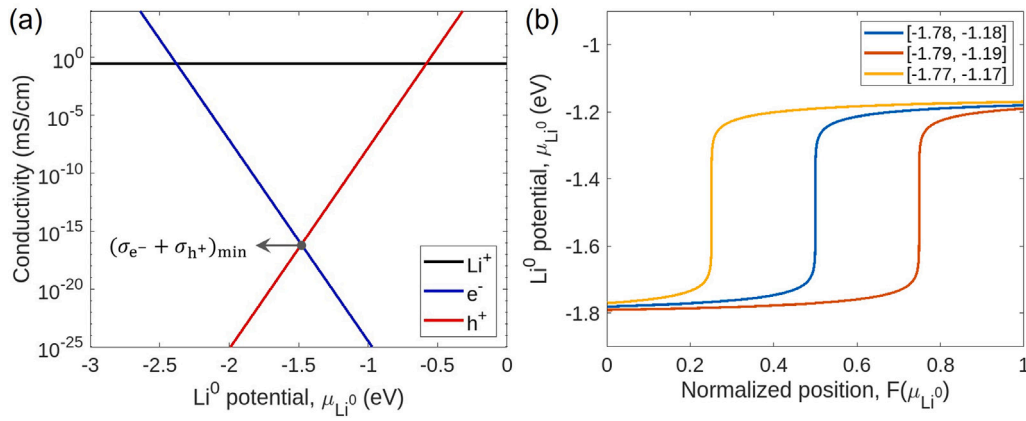


Fig. 2. Simulation of Li^0 potential distributions in 1D single-layer solid electrolytes without ionic bottlenecks under different applied boundary potentials. (a) Conductivities as a function of Li^0 potential used for the calculations. (b) Li^0 potential profile obtained through analytical calculations. Assumptions for the calculations are as follows: Temperature $T = 298$ K, thickness $L = 100$ μm , and Li^0 potentials ranging from $-eU_{\text{cathode}}$ to $-eU_{\text{anode}}$ along the distance x from the left electrode, denoted as $[-eU_{\text{cathode}}, -eU_{\text{anode}}]$, with units omitted for simplicity in the legend.

the constant- σ_{Li^+} assumption, as rendered by the black line in Fig. 2a, breaks down. In addition to such kinetic transitions, when μ_{Li^0} swings too far away from the center of the triangle in either the oxidation (right) or reduction (left) direction, phase transitions can happen due to exceeding the thermodynamic electrochemical stability window, which will certainly change σ_{Li^+} as well. These caveats qualify the nearly constant σ_{Li^+} approximation rendered in Fig. 2a.

The asymmetry in the analytical structure between the majority, ionic disorder and minority, electronic disorders in nominally good SE can be seen from the Gibbs–Duhem equation as well. We group all majority ionic disorders into a concentration vector c_{ionic} , and minority electronic disorders as a 2D concentration vector $c_{\text{electronic}}$. We generally have $c_{\text{ionic}} \cdot d\mu_{\text{ionic}} + c_{\text{electronic}} \cdot d\mu_{\text{electronic}} = 0$ under constant T and P as we scan different x of the SE. With c_{ionic} including mobile Li^+ at least several orders of magnitude greater than $c_{\text{electronic}}$, there must be $|\nabla\mu_{\text{ionic}}| \ll |\nabla\mu_{\text{electronic}}|$. Since $\mu_{\text{Li}^+} + \mu_{e^-} = \mu_{\text{Li}^0}$, the sharp gradient in $\mu_{e^-}(x)$ at the redox front—where the SE is turned from reduced (off-stoichiometry $\delta(x) > 0$) to oxidized (off-stoichiometry $\delta(x) < 0$), just as the SE kinetically undergoes the electronic conductivity bottleneck—will be inherited by $\mu_{\text{Li}^0}(x)$ as well. The above is the chemical potential situation. The electrostatic potential situation is much gentler: since j_{Li^+} must remain divergence-free and therefore an exact spatial constant at steady state, if one is to avoid Faradaic decomposition of SE, there cannot be a sharp gradient anywhere in the electrostatic potential. Indeed, the electrostatic potential gradient is constant everywhere when exact electroneutrality is demanded in a 1D single crystal, as rendered in Fig. S1a by the requirement of Poisson’s equation; and $\mu_{\text{Li}^+}(x)$, as plotted in Fig. S1b, also shows no sharp gradients out of the numerical solution, even though $\mu_{\text{Li}^0}(x)$ varied drastically at the redox front of the SE (Fig. S1c).

Thus, for the calculations in Fig. 2b, the conductivities are assumed to follow the diagram shown in Fig. 2a, which is a modified version of Fig. 1a in Ref. [10], with the reference potential of μ_{Li^0} adjusted so that μ_{Li^0} in Li_{BCC} becomes 0 eV. This ensures that the electronic potential U vs. Li/Li^+ satisfies $eU = -\mu_{\text{Li}^0}$ when converted using the Nernst equation. Different boundary potentials are assumed, causing μ_{Li^0} to vary from $-eU$ at the cathode to that at the anode (i.e., from $-eU_{\text{cathode}}$ to $-eU_{\text{anode}}$) along the distance x from the left electrode, denoted as $[-eU_{\text{cathode}}, -eU_{\text{anode}}]$, with units omitted for simplicity (e.g., $[-3, 0]$). Throughout the study, the temperature, current density, and thickness of the SE separator are assumed to be 298 K, 1 mA/cm^2 , and 100 μm , respectively. The t_{Li} values for the three boundary potential pairs tested in Fig. 2b are essentially 1, differing only in the eleventh decimal place.

Regardless of the boundary potentials, the μ_{Li^0} profiles in Fig. 2b exhibit one rapid increase, referred to as μ_{Li^0} jumps, which are found to

be responsible for the transverse degradation, as outlined in Section 2.1. These jumps are attributed to the generic electronic bottleneck [11], $(\sigma_{e^-} + \sigma_{h^+})_{\text{min}}$, where the curves for σ_{e^-} and σ_{h^+} intersect as marked by an arrow in Fig. 2a. Specifically, the flux of a charged species (R^n , where n is the net charge of the species) is proportional to the gradient in its electrochemical potential ($\nabla\tilde{\mu}_{R^n}$, where $\tilde{\mu}_{R^n} = \mu_{R^n} + ne\phi$, e is the elementary charge, and ϕ is the electrostatic potential). Since Li^+ has a little gradient in chemical potential (i.e., $\nabla\mu_{\text{Li}^+} \approx 0$), its flow is driven mostly by the gradient in ϕ , while e^-/h^+ flow is driven by gradients in both μ_{e^-} and ϕ . To maintain a constant e^-/h^+ flow across the electronic bottleneck at steady state, a jump in μ_{e^-} and/or ϕ is required. Since there should be no jump in ϕ to maintain a constant Li^+ flow, jumps in μ_{e^-} occur, leading to a corresponding jump in μ_{Li^0} to satisfy the local equilibrium described by Eq. (3).

The position of transport bottleneck-induced potential jumps is highly sensitive to the relative shift of boundary potentials with respect to μ_{Li^0} at $(\sigma_{e^-} + \sigma_{h^+})_{\text{min}}$, as shown in Fig. 2b, which aligns with the results in Fig. 2c of Ref. [10] obtained through numerical calculations. Increasing the boundary potentials by 0.01 eV, which shifts the asymmetry toward higher potentials, causes the μ_{Li^0} jump to move leftward by 50%, from a normalized position of 0.5 to 0.25, as depicted by the yellow line. On the other hand, reducing the boundary potentials by 0.01 eV—shifting the asymmetry toward lower potentials—results in a shift of the μ_{Li^0} jump in the opposite direction (red line).

Fundamentally, this phenomenon arises from the highly nonlinear dependence of electronic conductivity on μ_{Li^0} , shown in Eqs. (14) and (15). As a result, the potential jump often cannot be entirely eliminated just by avoiding μ_{Li^0} at $(\sigma_{e^-} + \sigma_{h^+})_{\text{min}}$. For example, if we assume a boundary potential range of $[-2.11, -1.51]$, the jump is pushed almost entirely to the right but still occurs at $x/L < 1$, as shown in Fig. S2. This happens because the electronic conductivity at $\mu_{\text{Li}^0} = -1.51$ eV is still several orders of magnitude smaller than that at $\mu_{\text{Li}^0} = -2.11$ eV and essentially functions as an electronic bottleneck although the μ_{Li^0} range within the SE set by the boundary potentials does not pass through μ_{Li^0} at $(\sigma_{e^-} + \sigma_{h^+})_{\text{min}}$ ($= -1.48$ eV in Fig. 2).

3.2. Marginalization of electronic bottleneck-induced potential jumps

The extreme sensitivity discussed in Section 3.1 suggests that detrimental potential jumps could be mitigated by engineering the effective conductivity across the SE separator—for example, by introducing a compositional gradient across a single type of SE or by constructing a multilayered separator with different SEs. Inspired by this observation, we next simulate various multilayering scenarios and discuss their implications on SE separators’ resistance to electrochemo-mechanical

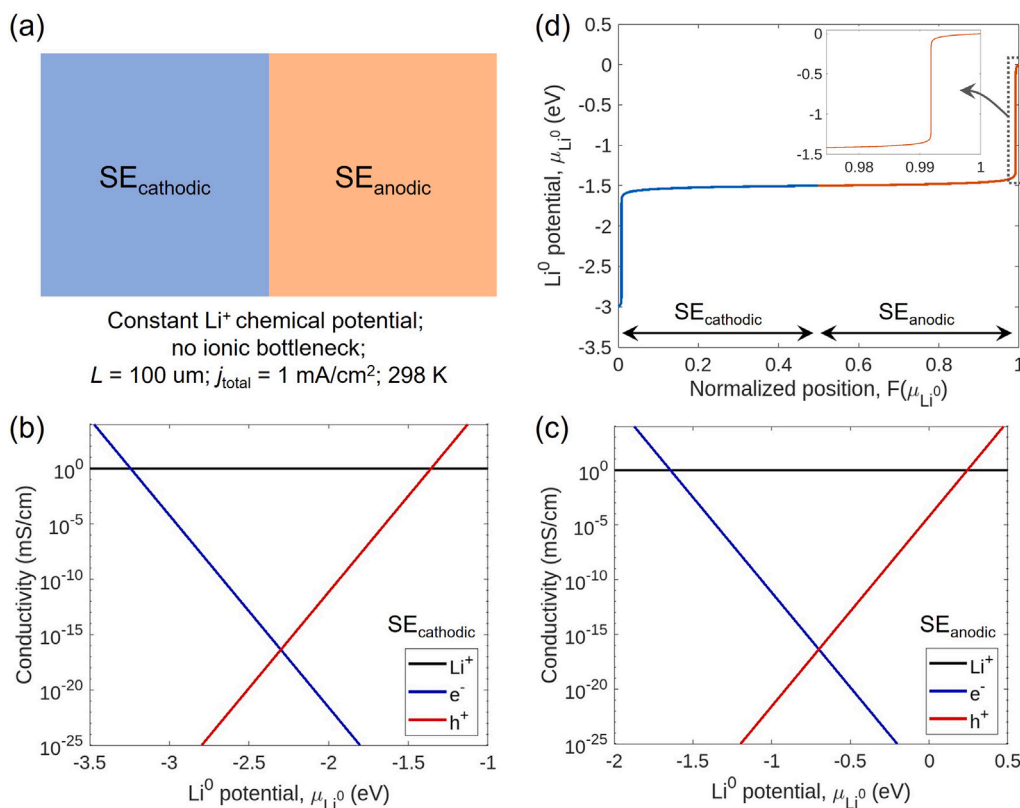


Fig. 3. Simulation of Li⁰ potential distribution in a bilayer SE separator without ionic bottlenecks. (a) Schematic diagram of the model SE separator comprising two SEs, denoted as SE_{cathodic} and SE_{anodic}, and simulation conditions. (b, c) Conductivity diagram as a function of Li⁰ potential for (b) SE_{cathodic} and (c) SE_{anodic}, respectively. (d) Li⁰ potential profile obtained through analytic calculations. The inset shows a magnified view of the dotted region with a potential jump. The applied boundary potentials are [-3, 0], and the corresponding t_{Li} is 0.9812.

degradation. Fig. 3a depicts a model SE separator consisting of two different SE layers with equal thickness. The SE near the cathode is denoted as SE_{cathodic}, and the one near the anode as SE_{anodic}. The Li⁺ chemical potential is considered constant across the layers, and the SE separator is assumed to be free of ionic bottlenecks, including at the interface.

Fig. 3b,c show the conductivity diagrams of hypothetical SE_{cathodic} and SE_{anodic}, respectively. We first discuss the μ_{Li⁰} range within which the SEs should be nominally good ionic conductors, where fast ion concentrations and conductivities remain nearly insensitive to redox conditions, while electronic conductivity varies with redox conditions. Assuming Li_{BCC} as an anode in direct contact with SE_{anodic}, the reductive stability (U_{lower}) of SE_{anodic} should preferably be ≤ 0 V vs. Li/Li⁺, corresponding to μ_{Li⁰} ≥ 0 eV. In contrast, the average operating voltage of layered oxide cathodes, such as LiNi_xMn_yCo_{1-x-y}O₂, is 3.9 V. Given a voltage gradient across the composite cathode, the oxidative stability (U_{upper}) of SE_{cathodic} should preferably be greater than ~3 V. For example, LLZO has been reported to have a U_{upper} of approximately 3 V (~2.9 V according to Ref. [24] and ~3.1 V according to Ref. [7]). In other words, SE_{cathodic} and SE_{anodic} are required to remain nominally good ionic conductors down to a μ_{Li⁰} of -3 eV and up to a μ_{Li⁰} of 0 eV, respectively.

Within this μ_{Li⁰} range, the Li⁺ conductivity of SE_{cathodic} and SE_{anodic} should then remain essentially constant, while their e⁻ and h⁺ conductivities are sufficiently low compared to Li⁺ conductivity. The Li⁺ conductivity of superionic conductors typically ranges from 10⁻⁴ mS/cm to 10 mS/cm at 298 K (e.g., 0.3 mS/cm for LLZO [25] and Li₇N₂I [17], 1 mS/cm for Li₆PS₅Cl [26], 10 mS/cm for Li₁₀GeP₂S₁₂ [27], and 0.4 mS/cm to 7 mS/cm for off-stoichiometric Li-Y-Cl-(Br) [28]). We thus assumed a Li⁺ conductivity of 1 mS/cm for both SE_{cathodic} and SE_{anodic} across a μ_{Li⁰} range of -4 to 1 eV for simplicity.

Experimentally measured electronic conductivities are also available for representative superionic conductors. However, these values are typically obtained using the Hebb-Wagner polarization method with ion-blocking electrodes, and thus only represent electronic conductivities at specific μ_{Li⁰} values. Therefore, electronic conductivities are assumed to be at least four orders of magnitude lower than Li⁺ conductivity within the given μ_{Li⁰} range, based on the practical requirement that SE separators must be fully charged within an hour and capable of holding the charge for 12 months. Accordingly, the parameter A in Eqs. (15) and (16) for both SEs is set to 4.25×10^{-17} , while B values are -2.3 eV and -0.7 eV for SE_{cathodic} and SE_{anodic}, respectively. A more detailed rationale for choosing these SE-specific constants is provided in Supplementary Note 1.

Fig. 3d shows the simulated μ_{Li⁰} profile in the bilayer SE separator. The boundary potentials of [-3, 0] are applied. Due to asymmetric boundary potentials relative to the μ_{Li⁰} at $(\sigma_{e^-} + \sigma_{h^+})_{min}$, the potential jumps induced by electronic bottlenecks are marginalized to the edges of the SE separator: $x/L < 0.01$ and > 0.99 , as shown in the inset with a magnified view. Near the surface, stress induced by lattice mismatch can be more easily relieved. Additionally, the lattice mismatch itself is milder, with the magnitude of the potential jumps in each SE halved compared to the single-layer SE separator. These factors indicate a reduced likelihood of destructive internal stress and transverse cracking. Furthermore, as the μ_{Li⁰} remains far from the boundary potentials throughout most of the SE separator, the probability of overshoots or undershoots is significantly reduced compared to single-layer SE separators, which tend to put nearly the entire separator at risk of overshoots or undershoots.

3.3. Incapacitation of ionic bottleneck-induced jumps

Dong et al. [11] have shown that the ionic bottlenecks in single-layer SEs can induce μ_{Li^0} jumps that exceed the boundary potential, as these are built upon a significant jump at the generic electronic bottleneck. The latter jump effectively transforms the anode and cathode sides of the SE into “virtual” electrodes, making both sides susceptible to μ_{Li^0} overshoots or undershoots beyond the μ_{Li^0} at the SE separator edges. Such behavior can lead to the formation of isolated Li_{Metal} islands or O_2 bubbles within the SE separator, potentially generating high local pressure, initiating transverse cracks, and facilitating the propagation of longitudinal cracks in the worst scenario.

Meanwhile, the marginalization of μ_{Li^0} jumps induced by electronic bottlenecks, as discussed in Section 3.1, suggests that μ_{Li^0} could remain moderate relative to the boundary potential throughout the SE separator. This moderation may prevent the μ_{Li^0} jumps caused by ionic bottlenecks from exceeding the boundary potential, thereby reducing the likelihood of such degradation. To further explore this, we model a bilayer SE separator with ionic bottlenecks and examine the impact of additional μ_{Li^0} jumps at these sites. Fig. 4a illustrates the model SE separators. The conditions are consistent with those in Fig. 3a, except that three ionic bottlenecks are introduced at x/L values of 0.25, 0.5, and 0.75. The boundary at $x/L = 0.5$ represents a phase boundary, while the other two correspond to grain boundaries. The ionic bottlenecks are assumed to have a normalized thickness ($\Delta x/L$) of 0.001, and numerical calculations are used to simplify the modeling of ionic bottlenecks. Fig. 4b–d depict the simulated μ_{Li^0} profiles. In Fig. 4b, the Li^+ conductivity of the first boundary ($\sigma_{\text{Li}^+}^{1\text{st}}$) is set to 10^{-4} of the lattice Li^+ conductivity ($\sigma_{\text{Li}^+}^{\text{lattice}}$), while those of the other boundaries ($\sigma_{\text{Li}^+}^{2\text{nd}}$ and $\sigma_{\text{Li}^+}^{3\text{rd}}$) are set to $10^{-2}\sigma_{\text{Li}^+}^{\text{lattice}}$. Similar conditions are applied in Fig. 4c,d, but with varying Li^+ conductivities at the second

and third boundaries, respectively—i.e., $\sigma_{\text{Li}^+}^{1\text{st}} = \sigma_{\text{Li}^+}^{3\text{rd}} = 10^{-2}\sigma_{\text{Li}^+}^{\text{lattice}}$ and $\sigma_{\text{Li}^+}^{2\text{nd}} = 10^{-4}\sigma_{\text{Li}^+}^{\text{lattice}}$ for Fig. 4c, and $\sigma_{\text{Li}^+}^{1\text{st}} = \sigma_{\text{Li}^+}^{2\text{nd}} = 10^{-2}\sigma_{\text{Li}^+}^{\text{lattice}}$ and $\sigma_{\text{Li}^+}^{3\text{rd}} = 10^{-4}\sigma_{\text{Li}^+}^{\text{lattice}}$ for Fig. 4d.

Unlike in single-layer SEs, where ionic bottlenecks tend to produce large μ_{Li^0} jumps that exceed boundary potentials (as shown by Fig. 3 in Ref. [11]), the jumps in all three cases remain within the boundary potentials. We attribute this difference to the marginalization of electronic bottlenecks, which keeps μ_{Li^0} moderate throughout the SE separator, preventing the several eV-level μ_{Li^0} jumps caused by the generic electronic bottleneck that the 0.1 eV-level jumps from ionic bottlenecks would otherwise amplify. As a result, the formation of Li_{Metal} islands or O_2 bubbles is effectively prevented. Meanwhile, it should be noted that potential jumps at ionic bottlenecks such as phase boundaries can induce a space charge layer, leading to capacitive behavior and contributing to the high interfacial impedance observed in multilayered SE separators. This effect may be either strengthened or weakened depending on the characteristics of the intrinsic space charge layer that forms due to defect equilibria, influenced by differences in the formation energies of individual defects, which drive deviations in ion concentrations at the surface compared to the bulk.

3.4. Effect of extrinsic factors: boundary potentials and relative thickness of each SE layer

The exact position of potential jumps is highly sensitive to boundary potentials. As a result, variations in boundary potentials can shift the μ_{Li^0} jump induced by generic electronic bottlenecks toward the center of the multilayered SE separator, leaving the SE separator still susceptible to both lattice mismatch-induced transverse cracking and overshoots/undershoots. To evaluate the tolerance of multilayering

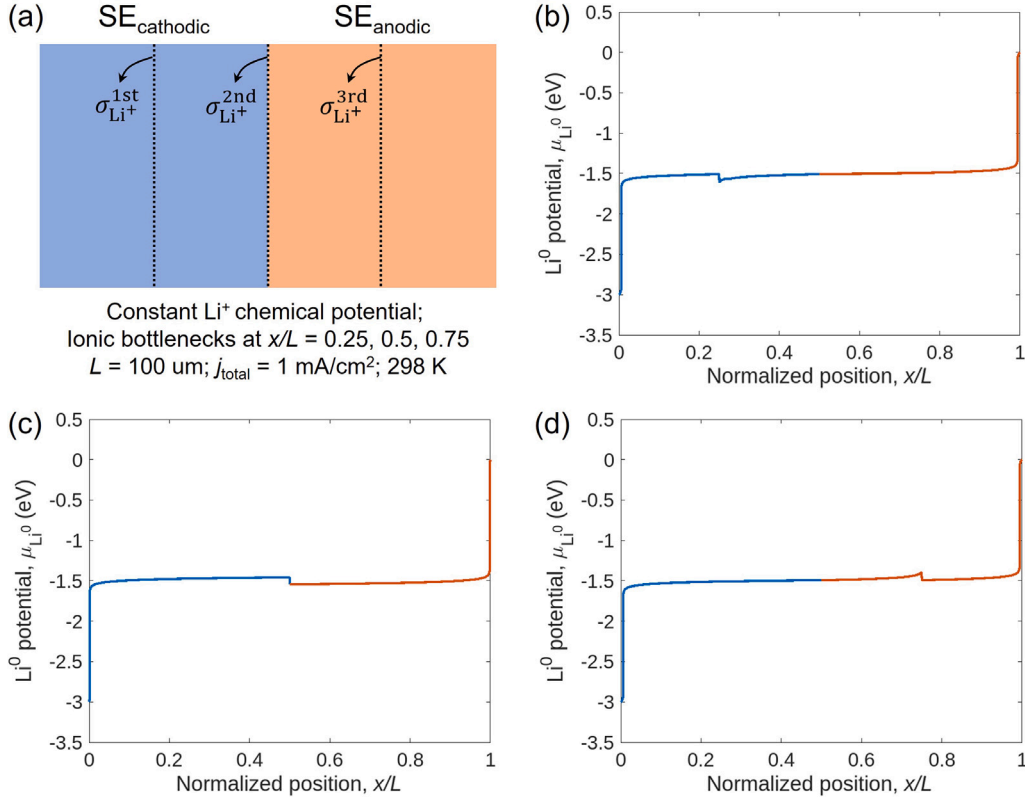


Fig. 4. Simulation of Li^0 potential in bilayer SE separators with ionic bottlenecks at $x/L = 0.25, 0.5$, and 0.75 . (a) Schematic diagram of the model SE separator and simulation conditions. Ionic conductivities at each bottleneck are $\sigma_{\text{Li}^+}^{1\text{st}}$, $\sigma_{\text{Li}^+}^{2\text{nd}}$, and $\sigma_{\text{Li}^+}^{3\text{rd}}$. (b–d) Li^0 potential profiles obtained through numerical calculations. One of the conductivities is set to $10^{-4}\sigma_{\text{Li}^+}^{\text{lattice}}$: (b) $\sigma_{\text{Li}^+}^{1\text{st}}$, (c) $\sigma_{\text{Li}^+}^{2\text{nd}}$, and (d) $\sigma_{\text{Li}^+}^{3\text{rd}}$. Those of the other bottlenecks are set to $10^{-2}\sigma_{\text{Li}^+}^{\text{lattice}}$, and the boundary potentials of $[-3, 0]$ are applied. The corresponding ν_{Li} values for (b–d) are 0.9735, 0.8902, and 0.9738, respectively.

strategies under asymmetric boundary conditions, we vary the boundary potentials. The model SE separators are the same as in Fig. 4a, except that the conductivities at each bottleneck are preset to $10^{-2}\sigma_{\text{Li}^+}^{\text{lattice}}$, $10^{-2}\sigma_{\text{Li}^+}^{\text{lattice}}$, and $10^{-4}\sigma_{\text{Li}^+}^{\text{lattice}}$ from the first to the third boundary, respectively.

Fig. 5a–c display the simulated μ_{Li^0} profiles for boundary potentials of $[-2.4, -eU_{\text{anode}}]$, with $-eU_{\text{anode}}$ varying from 0.05, 0.10, to 0.15 eV, respectively. Note that the reference state for μ_{Li^0} in all figures is the chemical potential of Li^0 atoms in the pure Li_{BCC} phase, which is considered infinitely large from an atomistic perspective. Therefore, μ_{Li^0} can exceed 0 (vs. $\text{Li}^+/\text{Li}_{\text{BCC}}$) when clusters of Li^0 atoms adopt atomic arrangements other than BCC or when BCC nuclei are nanoscale, where surface contributes to increasing the chemical potential of consisting Li^0 atoms (i.e., the Gibbs-Thomson effect). At $-eU_{\text{anode}} = 0.05$ eV, the position of the μ_{Li^0} jump caused by the generic electronic bottleneck in $\text{SE}_{\text{anodic}}$ shifts leftward, but the fraction of the SE separator susceptible to overshoot remains confined to an x/L of >0.95 . Thus, the statistical probability of having ionic bottlenecks within the vulnerable regions remains low, and the jump at $x/L = 0.75$ is still incapable of overshooting. Increasing $-eU_{\text{anode}}$ to 0.10 eV and 0.15 eV further shifts the several-eV jump caused by the generic electronic bottleneck toward the center of the SE separator, making a larger portion of $\text{SE}_{\text{anodic}}$ —and the entire $\text{SE}_{\text{anodic}}$ at 0.15 eV—subject to significantly reduced conditions and susceptible to overshoots. However, the magnitude of the jump induced by the ionic bottleneck at x/L remains mild and does not exceed the given boundary potentials. For comparison, the result corresponding to $-eU_{\text{anode}} = -0.8$ eV is also provided in Fig. S3. These results suggest that multilayering could enhance resistance to Li_{Metal} island formation within SE separators when appropriately designed. Particularly, when combined with an approach that tunes the

equilibrium voltage of anodes by a few hundred millivolts for instance, through alloying Li_{BCC} which induces a thermodynamic voltage shift comparable in magnitude to kinetically-induced potential jumps across transport bottlenecks such as grain boundaries, this strategy may help ensure that pure Li_{Metal} is never deposited at such bottlenecks.

Furthermore, the observation in Fig. 5c that the overshoot-vulnerable region is confined to $\text{SE}_{\text{anodic}}$ suggests that reducing the layer thickness could further decrease susceptibility. To investigate this, we examine the effect of the relative thickness of SE layers. Fig. 6a shows the model SE separators, with all conditions identical to those in Fig. 4a, except that $\text{SE}_{\text{cathodic}}$ now spans x/L from 0 to 0.75, while $\text{SE}_{\text{anodic}}$ spans from 0.75 to 1. Fig. 6b displays the simulated μ_{Li^0} profiles for boundary potentials of $[-3, 0.15]$. The position of the μ_{Li^0} jump caused by the generic electronic bottleneck in $\text{SE}_{\text{anodic}}$ shifts rightward compared to that in Fig. 5c. The extension of highly reduced regions is restricted within $\text{SE}_{\text{anodic}}$, keeping μ_{Li^0} in $\text{SE}_{\text{cathodic}}$ ($x/L < 0.75$) far from boundary potentials. Notably, a finite portion of $\text{SE}_{\text{anodic}}$ is also no longer susceptible to overshoot in contrast to the profile in Fig. 5c, where the entire $\text{SE}_{\text{anodic}}$ is potentially at risk. This indicates that a thinner layer of an additional SE may suffice—or even be more effective—in mitigating transport bottleneck-induced degradation. This finding significantly relaxes the σ_{Li^+} requirement for $\text{SE}_{\text{anodic}}$.

3.5. Effect of intrinsic factors: ionic and electronic conductivity, and Li^0 potential at the generic electronic bottleneck relative to boundary potentials

Next, we explore the effect of ionic and electronic conductivities on transport bottleneck-induced μ_{Li^0} jumps. The model SE separators are the same as in Fig. 6, except that the conductivities of $\text{SE}_{\text{anodic}}$ are varied. The boundary potentials are fixed at $[-2.4, 0.3]$. Fig. 7a presents

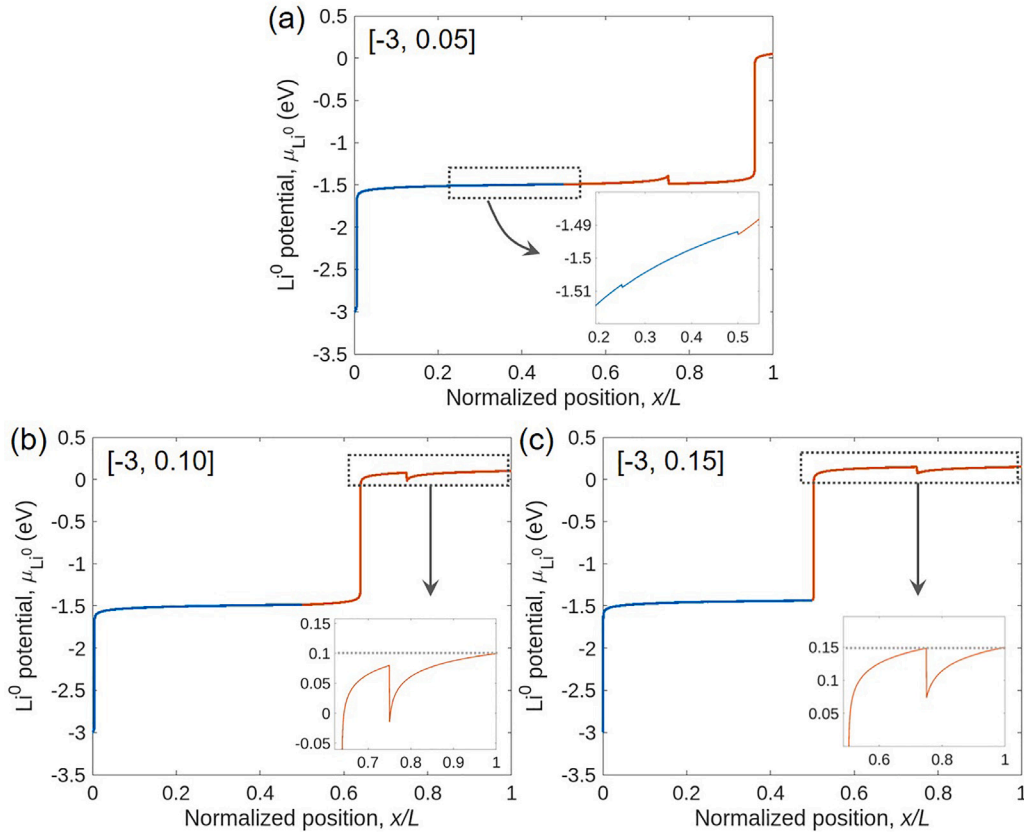


Fig. 5. The effect of boundary potentials on Li^0 potential profile in bilayer SE separators with ionic bottlenecks. The model SE separator is the same as in Fig. 4a. Ionic conductivities at each ionic bottleneck are as follows: $\sigma_{\text{Li}^+}^{\text{1st}} = \sigma_{\text{Li}^+}^{\text{2nd}} = 10^{-2}\sigma_{\text{Li}^+}^{\text{lattice}}$ and $\sigma_{\text{Li}^+}^{\text{3rd}} = 10^{-4}\sigma_{\text{Li}^+}^{\text{lattice}}$. The applied boundary potentials are as follows: (a) $[-3, 0.05]$, (b) $[-3, 0.10]$, and (c) $[-3, 0.15]$. The corresponding t_{Li} values for (b–d) are 0.9738, 0.9651, and 0.7534, respectively. The inset in (a) shows a magnified view of μ_{Li^0} profile at $x/L = 0.25$ and 0.5 , while the ones in (b) and (c) show the profiles at $x/L = 0.75$.

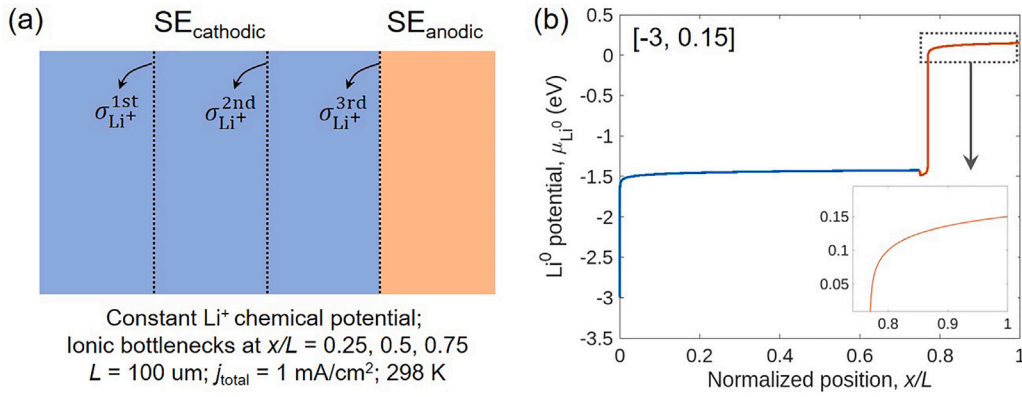


Fig. 6. The effect of the thickness ratio on Li^0 potential profile in a bilayer SE separator with ionic bottlenecks. (a) Schematic diagram of the model separator with a thickness ratio of 3:1 and simulation conditions. (b) Li^0 potential profiles obtained through numerical calculations. Ionic conductivities at each ionic bottleneck are as follows: $\sigma_{\text{Li}^+}^{\text{1st}} = \sigma_{\text{Li}^+}^{\text{2nd}} = 10^{-2} \sigma_{\text{Li}^+}^{\text{lattice}}$ and $\sigma_{\text{Li}^+}^{\text{3rd}} = 10^{-4} \sigma_{\text{Li}^+}^{\text{lattice}}$. The applied boundary potentials are $[-3, 0.15]$, and the corresponding t_{Li} value is 0.7218. The inset shows a magnified view of μ_{Li^0} profile near the edge of the SE separator, where μ_{Li^0} is close to the boundary potential, $-eU_{\text{anode}}$.

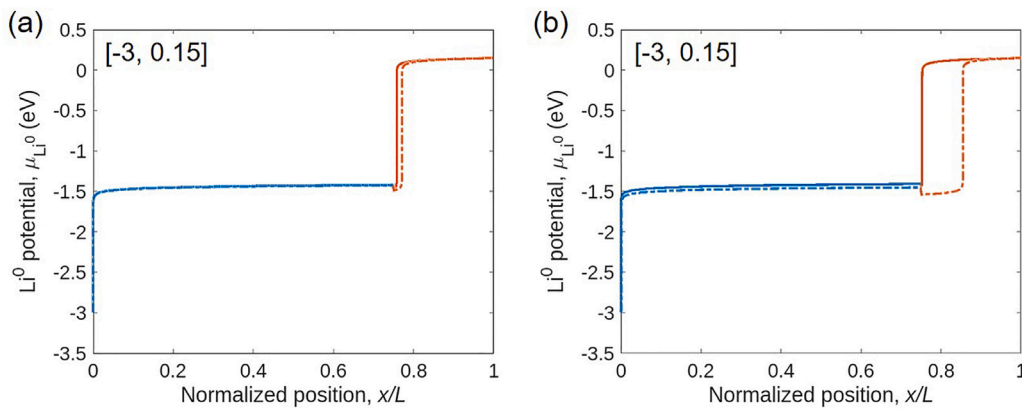


Fig. 7. The effect of ionic and electronic conductivities on Li^0 potential profile in bilayer SE separators with ionic bottlenecks. The model SE separator is the same as in Fig. 6a. Ionic conductivities at each ionic bottleneck are as follows: $\sigma_{\text{Li}^+}^{\text{1st}} = \sigma_{\text{Li}^+}^{\text{2nd}} = 10^{-2} \sigma_{\text{Li}^+}^{\text{lattice}}$ and $\sigma_{\text{Li}^+}^{\text{3rd}} = 10^{-4} \sigma_{\text{Li}^+}^{\text{lattice}}$. The applied boundary potentials are $[-3, 0.15]$. (a) Li^0 potential profiles obtained through numerical calculations under different σ_{Li^+} of $\text{SE}_{\text{anodic}}$ from 0.1 m/s (solid line) to 10 m/s (dotted line). The corresponding t_{Li} values are 0.6543 and 0.7280, respectively. (b) Li^0 potential profiles obtained through numerical calculations under different electronic conductivities of $\text{SE}_{\text{anodic}}$, doubled (solid line) or reduced to 20% (dotted line). The corresponding t_{Li} values are 0.4860 and 0.9124, respectively.

the simulated μ_{Li^0} profiles with varying σ_{Li^+} in $\text{SE}_{\text{anodic}}$, ranging from 10^{-1} (solid line) to 10^1 (dotted line). The μ_{Li^0} jumps shift outward as σ_{Li^+} increases, reducing the extent of the vulnerable regions, though the change is minimal. While low σ_{Li^+} is not particularly detrimental to the μ_{Li^0} profile, maintaining $\sigma_{\text{Li}^+} > 10^{-1}$ would still be desirable for both rate capability and achieving an ionic transference number (t_{ion}) close to 1, unless $\text{SE}_{\text{anodic}}$ is very thin. Fig. 7b shows the simulated μ_{Li^0} profiles when σ_{e^-} and σ_{h^+} in $\text{SE}_{\text{anodic}}$ are either doubled (solid line) or reduced to 20% (dotted line). As σ_{e^-} and σ_{h^+} decrease, the μ_{Li^0} jump induced by electronic bottlenecks shifts rightward, reducing the susceptible regions. This suggests that minimizing electronic conductivity can help marginalize potential jumps induced by generic electronic bottlenecks, even under highly asymmetric boundary potentials.

Lastly, we examine the effect of Li^0 potentials at the generic electronic bottleneck ($\mu_{\text{Li}^0}^{\text{GEB}}$) relative to the boundary potentials. The model SE separators remain consistent with Fig. 3a, except for variations in $\mu_{\text{Li}^0}^{\text{GEB}}$. In Fig. 3, the $\mu_{\text{Li}^0}^{\text{GEB}}$ values of $\text{SE}_{\text{cathodic}}$ and $\text{SE}_{\text{anodic}}$ are -2.3 eV and -0.7 eV, as shown in Fig. 3b and c, respectively, while the boundary potentials are set to $[-3, 0]$. In Fig. 8, the boundary potentials remain unchanged, but the $\mu_{\text{Li}^0}^{\text{GEB}}$ values of $\text{SE}_{\text{cathodic}}$ and $\text{SE}_{\text{anodic}}$ vary as follows: $(-2.3, -0.8)$, $(-2.2, -0.8)$, $(-2.4, -0.8)$, and $(-2.3, -0.6)$ in units of eV for Fig. 8a–d. These variations result in different Li^0 potentials at the phase boundary between the two SEs ($x/L = 0.5$): -1.5000 , -1.4998 , -1.5917 , and -1.4500 eV in Fig. 8a–d, respectively.

The asymmetry of Li^0 potentials at the edge of each SE, relative to the $\mu_{\text{Li}^0}^{\text{GEB}}$ values of $\text{SE}_{\text{cathodic}}$ and $\text{SE}_{\text{anodic}}$, significantly influences the

μ_{Li^0} profile within the SE separators. Specifically, reducing the $\mu_{\text{Li}^0}^{\text{GEB}}$ of $\text{SE}_{\text{anodic}}$ from -0.7 eV to -0.8 eV—i.e., shifting $\mu_{\text{Li}^0}^{\text{GEB}}$ inward with respect to boundary potentials—pushes the Li^0 potential asymmetry in $\text{SE}_{\text{anodic}}$ toward higher potentials. This adjustment moves the μ_{Li^0} jump at the generic electronic bottleneck in $\text{SE}_{\text{anodic}}$ leftward, closer to the phase boundary between the two SEs (Fig. 8a), thereby exposing half of the SE separator to possible overshoots. Conversely, increasing the $\mu_{\text{Li}^0}^{\text{GEB}}$ of $\text{SE}_{\text{cathodic}}$ by $+0.1$ eV—i.e., shifting $\mu_{\text{Li}^0}^{\text{GEB}}$ inward—moves the μ_{Li^0} jump at the generic electronic bottleneck in $\text{SE}_{\text{cathodic}}$ rightward, making the profile resemble that of a single-layer SE separator (Fig. 2b), thus putting both SEs at risk. On the other hand, shifting the $\mu_{\text{Li}^0}^{\text{GEB}}$ outward—by reducing that of $\text{SE}_{\text{cathodic}}$ to -2.4 eV or increasing that of $\text{SE}_{\text{anodic}}$ to -0.6 eV—also pushes the μ_{Li^0} jumps toward the SE separator edges, thereby mitigating the risk of transverse degradation and potentially reducing longitudinal degradation as well. While electronic conductivity diagrams have not been widely investigated for Li-ion conductors, our observations underscore the need for experimental studies to quantify the realistic SE-specific constants A and B ($\equiv \mu_{\text{Li}^0}^{\text{GEB}}$) in Eqs. (14) and (15) across different SE materials.

4. Discussion

Achieving stable cycling without externally applied stack pressure is a key milestone for the practical feasibility of ASSBs, as maintaining

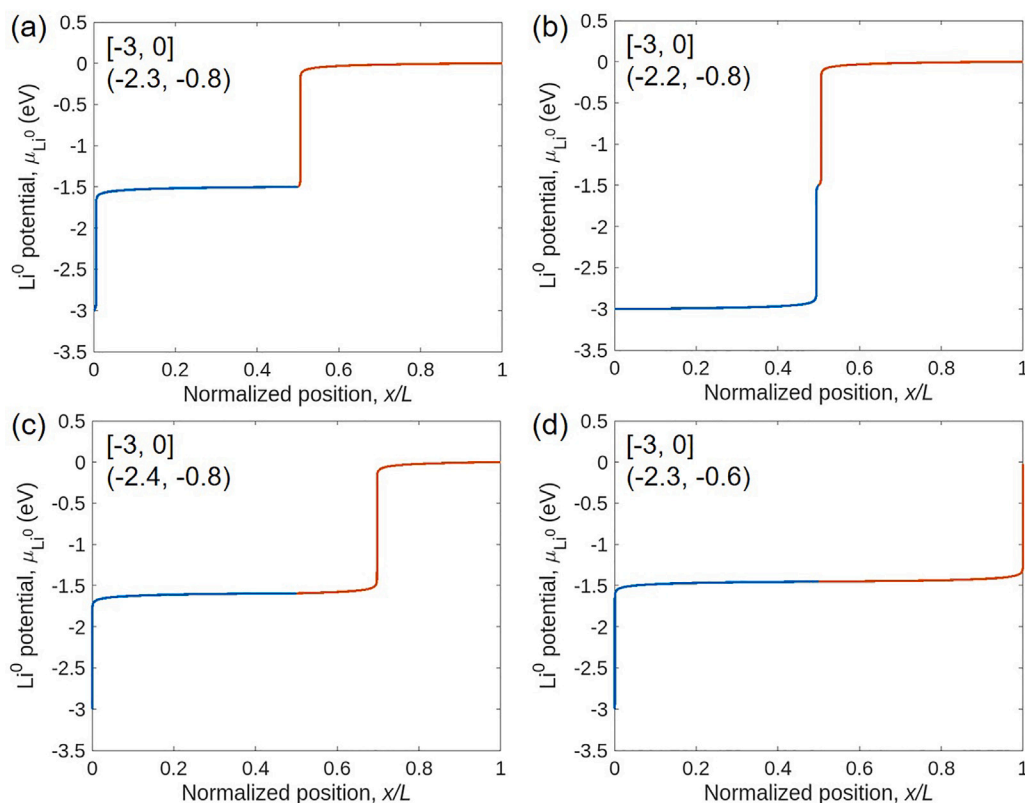


Fig. 8. The effect of Li^0 potential at the generic electronic bottleneck relative to boundary potentials in bilayer SE separators without ionic bottlenecks. The model SE separator is the same as in Fig. 3a. The applied boundary potentials are $[-3, 0]$. (a–d) Li^0 potential profiles obtained through numerical calculations. The $\mu_{\text{Li}^0}^{\text{GEB}}$ values of $\text{SE}_{\text{cathodic}}$ and $\text{SE}_{\text{anodic}}$ are as follows: (a) $(-2.3, -0.8)$, (b) $(-2.2, -0.8)$, (c) $(-2.4, -0.8)$, and (d) $(-2.3, -0.6)$. The corresponding t_{Li} values for (a–d) are 0.9947, 0.9947, 0.9926, and 0.9614, respectively.

sufficient physical contact among solid components becomes challenging. In the absence of applied pressure, only hydrostatic compressive stress of 0.1 MPa from atmospheric pressure and *in operando* generated stresses within the solid components are present. The latter stresses arise either externally due to volume or shape changes in other solid components, such as cathodes and/or anodes and the penetration of Li dendrites, or internally from marginal yet concentrated composition changes or evolution of Li metal islands, as observed in SEs. Locally, these stresses can become large enough to fracture the SEs [3,21]. The sum of these stress tensors and the resulting traction forces at any internal cross-sectional surfaces must remain below the local binding forces to maintain the initial arrangement.

When plastic deformability is limited and intrinsic toughening mechanisms are lacking, as in most ceramic SEs, keeping maximum stress as low as possible is crucial. Eq. (17) suggests that increasing separator thickness (L) and reducing current density (j_{total}) can mitigate lattice mismatch at the generic electronic bottleneck. However, these measures compromise energy density and rate capability, which are important performance metrics. Additionally, increasing pellet density and reducing grain boundaries can minimize ionic and electronic bottlenecks, reducing the statistical probability of overshoots/undershoots. Yet, such measures often require prolonged high-temperature processing, complicating manufacturing.

In this regard, our modeling results demonstrate the potential of multilayering SE separators as an alternative strategy for enhancing cycling stability under pressure-less conditions, as summarized in Fig. 9. First, multilayering SEs can divide a single large potential jump observed in single-layer SEs (Fig. 9a) into two smaller jumps, mitigating lattice mismatches and reducing the maximum accessible stress (Fig. 9b). Second, multilayering can confine detrimental μ_{Li^0} jumps induced by generic electronic bottlenecks to the edges of the SE separator, where stress from lattice mismatches—between highly reduced and

highly oxidized SEs—can be more easily relieved (Fig. 9c). Third, this confinement keeps μ_{Li^0} across much of the SE separator sufficiently distant from boundary potentials, preventing harmful overshoots/undershoots (Fig. 9c). This suppression reduces the likelihood of forming isolated Li_{Metal} or gaseous species like O_2 , which could otherwise induce transverse degradation via internal hydrostatic pressure or accelerate longitudinal degradation by connecting with penetrating Li_{Metal} dendrites.

This approach may become even more useful when employing nitride-, sulfide-, or halide-based SEs. These SEs are typically cold-sinterable, unlike oxide-based SEs, which require high-temperature, long-duration processing. However, when only cold-sintering is applied, these SEs generally exhibit high porosity compared to oxide-based SEs. This characteristic has been a significant challenge, limiting the investigation of the pressure-less capability of SE separators made from these materials, as it allows liquid catholyte penetration through interconnected pores, potentially leading to mechanical failure. Recent advances in solid-state ceramic catholytes capable of accommodating cathode volume changes pave the way for new investigations into these SEs' pressure-less capability [29]. That said, full-cell operation with non-oxide-based SE separators under pressure-less conditions has yet to be fully demonstrated to the best of the authors' knowledge, and the high density of transport bottlenecks after cold-sintering, along with the resulting susceptibility to both transverse and longitudinal degradation, is likely to keep posing a major challenge.

In the meantime, these SEs have already often been combined into multilayered structures. For example, nitride-based SEs with good reductive stability but limited oxidative stability have been paired with halide-based SEs that offer good oxidative stability but limited reductive stability to achieve a broader electrochemical window [30], while sulfide-based SEs are layered to prevent longitudinal crack and dendrite

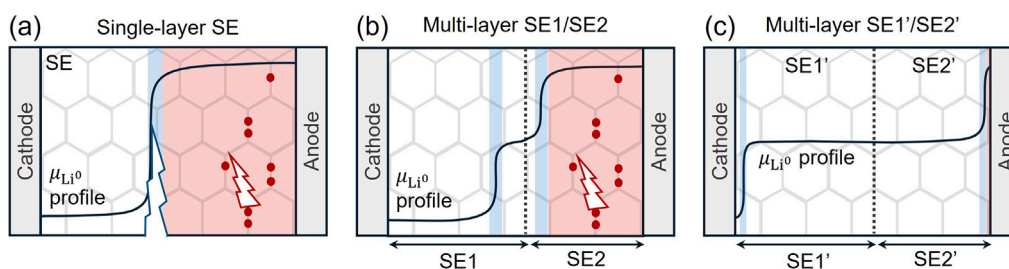


Fig. 9. Schematic illustration of Li^0 potential profiles in different SE separator configurations. (a) Single-layer SE separator with a single large potential jump, making it susceptible to transverse cracking due to lattice mismatch at the electronic bottleneck, as well as Li metal island formation at the ionic bottleneck and the resulting cracks. (b) Multilayered SE separator with two smaller, split potential jumps, which reduces susceptibility to transverse cracking from lattice mismatch but remains vulnerable to Li metal island formation and the associated cracks. (c) Multilayered SE separator where the two split potential jumps are pushed to the edges of the separator, reducing the propensity for both transverse cracking from lattice mismatch and detrimental Li metal island formation.

propagation [16]. As such, multilayering approaches have proven effective in ensuring electrochemical stability in high-energy-density ASSBs with high-voltage cathodes, as well as in creating short-circuit-proof SE separators, even in the presence of dendrites.

Hence, the current finding that multilayering can mitigate transverse degradation—while also delaying longitudinal degradation—suggests it could serve as an all-in-one strategy for advanced ASSBs, achieving high energy density and cycling stability under pressure-less conditions. Moreover, the investigated effects of various factors provide valuable design guidelines. Specifically, the results highlight the Li^0 potential at the generic electronic bottleneck ($\mu_{\text{Li}^0}^{\text{GEB}}$) as a key design metric for multilayered SE separators: the closer $\mu_{\text{Li}^0}^{\text{GEB}}$ is to the Li^0 potential at the electrodes, the nearer the potential jumps occur to the electrodes. Furthermore, the additional SE layer does not need to be as thick as the primary SE, alleviating the ionic conductivity constraint. Meanwhile, its electronic conductivity should be kept as low as possible, and microstructural features such as grain boundaries should be minimized to enhance resistance against Li metal island formation.

While adding extra layers may not be ideal from a manufacturing standpoint, the multi-faceted advantages may make multilayering a practically meaningful approach. Moreover, the fact that even a thin layer can suffice (or be more effective) is encouraging, as it minimizes energy density sacrifices. Lastly, the sensitivity of μ_{Li^0} jumps induced by generic electronic bottlenecks to the relative position of $\mu_{\text{Li}^0}^{\text{GEB}}$ values with respect to boundary potentials indicates that comparing the electrochemo-mechanical behavior of SE separators among cells with different cathode, anode, and SE combinations, as well as at different states of charge, is non-trivial. However, the observation that multilayering can confine the impact of boundary potential set by one electrode to the adjacent SE layer suggests it can minimize cross-talk between electrodes, enabling better control of hidden variables beyond those of immediate interest.

5. Conclusions

Our thermodynamic analysis has revealed the potential advantages of multilayering in mitigating transverse degradation, emphasizing the importance of redox-sensitive electronic conductivity in the electrochemo-mechanical degradation of SEs. Specifically, we derived a closed-form analytical solution for the Li^0 chemical potential within solid electrolyte separators and confirmed that the potential jump at the generic electronic bottleneck is highly sensitive to the asymmetry of boundary potentials relative to the Li^0 chemical potential at the generic electronic bottleneck. Building on this sensitivity, we proposed that these jumps can be confined to the edges of the SE separator, where they are less damaging, by tailoring the dependence of electronic conductivity on the Li^0 chemical potential. We also found that this confinement helps prevent the formation of isolated Li metal within

the separator, which can result from Li^0 chemical potential overshoots at transport bottlenecks such as grain boundaries.

While the effectiveness of confining potential jumps may be reduced under extreme boundary potentials, appropriate multilayering can still limit the damage to a single SE layer even in such cases. Moreover, this mitigation strategy remains effective and can be further enhanced even when the secondary SE layer is thin, particularly if it exhibits high ionic conductivity and extremely low electronic conductivity. These findings are important for enabling pressure-less capability, becoming especially critical when using cold-sintered solid electrolytes with relatively high porosity. Given that multilayering of SE separators has already been a common approach for addressing other forms of degradation, a comprehensive design of multilayered solid electrolyte separators could be highly impactful. In this context, this work provides theoretical guidelines for future efforts to address both transverse and longitudinal electrochemo-mechanical degradation in solid electrolytes.

CRediT authorship contribution statement

So Yeon Kim: Writing – review & editing, Writing – original draft, Visualization, Methodology, Investigation, Formal analysis, Conceptualization. **Ju Li:** Writing – review & editing, Supervision, Funding acquisition.

Declaration of competing interest

The authors declare that they have no known competing financial interests or personal relationships that could have appeared to influence the work reported in this paper.

Acknowledgments

We acknowledge support by DARPA, MINT program under contract number HR001122C0097 and the Samsung Advanced Institute of Technology. S.Y.K gratefully acknowledges support from the Kwanjeong Fellowship.

Appendix A. Supplementary data

Supplementary material related to this article can be found online at <https://doi.org/10.1016/j.actamat.2025.120982>.

References

- [1] Q. Zhao, S. Stalin, C.-Z. Zhao, L.A. Archer, Designing solid-state electrolytes for safe, energy-dense batteries, *Nat. Rev. Mater.* 5 (3) (2020) 229–252, <http://dx.doi.org/10.1038/s41578-019-0165-5>, Publisher: Nature Publishing Group URL <https://www.nature.com/articles/s41578-019-0165-5>.
- [2] J. Kasemchainan, S. Zekoll, D. Spencer Jolly, Z. Ning, G.O. Hartley, J. Marrow, P.G. Bruce, Critical stripping current leads to dendrite formation on plating in lithium anode solid electrolyte cells, *Nat. Mater.* 18 (10) (2019) 1105–1111, <http://dx.doi.org/10.1038/s41563-019-0438-9>, Publisher: Nature Publishing Group URL <https://www.nature.com/articles/s41563-019-0438-9>.

- [3] Z. Ning, D.S. Jolly, G. Li, R. De Meyere, S.D. Pu, Y. Chen, J. Kasemchainan, J. Ihli, C. Gong, B. Liu, D.L.R. Melvin, A. Bonnin, O. Magdysyuk, P. Adamson, G.O. Hartley, C.W. Monroe, T.J. Marrow, P.G. Bruce, Visualizing plating-induced cracking in lithium-anode solid-electrolyte cells, *Nat. Mater.* 20 (8) (2021) 1121–1129, <http://dx.doi.org/10.1038/s41563-021-00967-8>, Publisher: Nature Publishing Group URL <https://www.nature.com/articles/s41563-021-00967-8>.
- [4] Z. Ning, G. Li, D.L.R. Melvin, Y. Chen, J. Bu, D. Spencer-Jolly, J. Liu, B. Hu, X. Gao, J. Perera, C. Gong, S.D. Pu, S. Zhang, B. Liu, G.O. Hartley, A.J. Bodey, R.I. Todd, P.S. Grant, D.E.J. Armstrong, T.J. Marrow, C.W. Monroe, P.G. Bruce, Dendrite initiation and propagation in lithium metal solid-state batteries, *Nature* 618 (7964) (2023) 287–293, <http://dx.doi.org/10.1038/s41586-023-05970-4>, Publisher: Nature Publishing Group URL <https://www.nature.com/articles/s41586-023-05970-4>.
- [5] G. McConohy, X. Xu, T. Cui, E. Barks, S. Wang, E. Kaeli, C. Melamed, X.W. Gu, W.C. Chueh, Mechanical regulation of lithium intrusion probability in garnet solid electrolytes, *Nat. Energy* 8 (3) (2023) 241–250, <http://dx.doi.org/10.1038/s41560-022-01186-4>, Publisher: Nature Publishing Group URL <https://www.nature.com/articles/s41560-022-01186-4>.
- [6] Y. Zhu, X. He, Y. Mo, First principles study on electrochemical and chemical stability of solid electrolyte–electrode interfaces in all-solid-state Li-ion batteries, *J. Mater. Chem. A* 4 (9) (2016) 3253–3266, <http://dx.doi.org/10.1039/C5TA08574H>, Publisher: Royal Society of Chemistry URL <https://pubs.rsc.org/en/content/articlelanding/2016/ta/c5ta08574h>.
- [7] W.D. Richards, L.J. Miara, Y. Wang, J.C. Kim, G. Ceder, Interface Stability in Solid-State Batteries, *Chem. Mater.* 28 (1) (2016) 266–273, <http://dx.doi.org/10.1021/acs.chemmater.5b04082>, Publisher: American Chemical Society.
- [8] Y. Dong, I.-W. Chen, J. Li, Transverse and Longitudinal Degradations in Ceramic Solid Electrolytes, *Chem. Mater.* 34 (13) (2022) 5749–5765, <http://dx.doi.org/10.1021/acs.chemmater.2c00329>, Publisher: American Chemical Society.
- [9] M.S. Diallo, T. Shi, Y. Zhang, X. Peng, I. Shozib, Y. Wang, L.J. Miara, M.C. Scott, Q.H. Tu, G. Ceder, Effect of solid-electrolyte pellet density on failure of solid-state batteries, *Nat. Commun.* 15 (1) (2024) 858, <http://dx.doi.org/10.1038/s41467-024-45030-7>, Publisher: Nature Publishing Group URL <https://www.nature.com/articles/s41467-024-45030-7>.
- [10] Y. Zhang, Y. Dong, J. Li, Electrochemical shock and transverse cracking in solid electrolytes, *Acta Mater.* 265 (2024) 119620, <http://dx.doi.org/10.1016/j.actamat.2023.119620>, URL <https://linkinghub.elsevier.com/retrieve/pii/S1359645423009485>.
- [11] Y. Dong, Z. Zhang, A. Alvarez, I.-W. Chen, Potential jumps at transport bottlenecks cause instability of nominally ionic solid electrolytes in electrochemical cells, *Acta Mater.* 199 (2020) 264–277, <http://dx.doi.org/10.1016/j.actamat.2020.08.017>, URL <https://www.sciencedirect.com/science/article/pii/S1359645420306145>.
- [12] Q. Tu, T. Shi, S. Chakravarthy, G. Ceder, Understanding metal propagation in solid electrolytes due to mixed ionic-electronic conduction, *Matter* 4 (10) (2021) 3248–3268, <http://dx.doi.org/10.1016/j.matt.2021.08.004>, URL <https://linkinghub.elsevier.com/retrieve/pii/S2590238521003970>.
- [13] H. Liu, Y. Chen, P.-H. Chien, G. Amouzandeh, D. Hou, E. Truong, I.P. Oyekunle, J. Bhagu, S.W. Holder, H. Xiong, et al., Dendrite formation in solid-state batteries arising from lithium plating and electrolyte reduction, *Nat. Mater.* 24 (4) (2025) 1–8, <http://dx.doi.org/10.1038/s41563-024-02094-6>, Publisher: Nature Publishing Group URL <https://www.nature.com/articles/s41563-024-02094-6>.
- [14] S.Y. Kim, J. Li, Porous Mixed Ionic Electronic Conductor Interlayers for Solid-State Batteries, *Energy Mater. Adv.* 2021 (2021) <http://dx.doi.org/10.34133/2021/1519569>.
- [15] Y.-G. Lee, S. Fujiki, C. Jung, N. Suzuki, N. Yashiro, R. Omoda, D.-S. Ko, T. Shiratsuchi, T. Sugimoto, S. Ryu, J.H. Ku, T. Watanabe, Y. Park, Y. Aihara, D. Im, I.T. Han, High-energy long-cycling all-solid-state lithium metal batteries enabled by silver–carbon composite anodes, *Nat. Energy* 5 (4) (2020) 299–308, <http://dx.doi.org/10.1038/s41560-020-0575-z>, Publisher: Nature Publishing Group URL <https://www.nature.com/articles/s41560-020-0575-z>.
- [16] L. Ye, X. Li, A dynamic stability design strategy for lithium metal solid state batteries, *Nature* 593 (7858) (2021) 218–222, <http://dx.doi.org/10.1038/s41586-021-03486-3>, Publisher: Nature Publishing Group URL <https://www.nature.com/articles/s41586-021-03486-3>.
- [17] Z. Wang, J. Xia, X. Ji, Y. Liu, J. Zhang, X. He, W. Zhang, H. Wan, C. Wang, Lithium anode interlayer design for all-solid-state lithium-metal batteries, *Nat. Energy* 9 (3) (2024) 251–262, <http://dx.doi.org/10.1038/s41560-023-01426-1>, Publisher: Nature Publishing Group URL <https://www.nature.com/articles/s41560-023-01426-1>.
- [18] B. Hu, S. Zhang, Z. Ning, D. Spencer-Jolly, D.L.R. Melvin, X. Gao, J. Perera, S.D. Pu, G.J. Rees, L. Wang, L. Yang, H. Gao, S. Marathe, G. Burca, T.J. Marrow, P.G. Bruce, Deflecting lithium dendritic cracks in multi-layered solid electrolytes, *Joule* (2024) <http://dx.doi.org/10.1016/j.joule.2024.06.024>, Publisher: Elsevier URL [https://www.cell.com/joule/abstract/S2542-4351\(24\)00300-3](https://www.cell.com/joule/abstract/S2542-4351(24)00300-3).
- [19] F. Tietz, D. Sebold, A. Brisse, J. Scheffold, Degradation phenomena in a solid oxide electrolysis cell after 9000 h of operation, *J. Power Sources* 223 (2013) 129–135, <http://dx.doi.org/10.1016/j.jpowsour.2012.09.061>, URL <https://www.sciencedirect.com/science/article/pii/S0378775312014826>.
- [20] Y. Dong, I.-W. Chen, Oxygen potential transition in mixed conducting oxide electrolyte, *Acta Mater.* 156 (2018) 399–410, <http://dx.doi.org/10.1016/j.actamat.2018.06.014>, URL <https://www.sciencedirect.com/science/article/pii/S1359645418304828>.
- [21] J. Zhao, Y. Tang, Q. Dai, C. Du, Y. Zhang, D. Xue, T. Chen, J. Chen, B. Wang, J. Yao, N. Zhao, Y. Li, S. Xia, X. Guo, S.J. Harris, L. Zhang, S. Zhang, T. Zhu, J. Huang, In situ Observation of Li Deposition-Induced Cracking in Garnet Solid Electrolytes, *Energy & Environmental Materials* 5 (2) (2022) 524–532, <http://dx.doi.org/10.1002/eem2.12261>, eprint: <https://onlinelibrary.wiley.com/doi/pdf/10.1002/eem2.12261> URL <https://onlinelibrary.wiley.com/doi/abs/10.1002/eem2.12261>.
- [22] J. Maier, *Physical chemistry of ionic materials: ions and electrons in solids*, John Wiley & Sons, 2023.
- [23] Y. Dong, L. Qi, A. Alvarez, J. Li, I.-W. Chen, Enhanced mobility of cations and anions in the redox state: The polaronium mechanism, *Acta Mater.* 232 (2022) 117941, <http://dx.doi.org/10.1016/j.actamat.2022.117941>, URL <https://linkinghub.elsevier.com/retrieve/pii/S1359645422003226>.
- [24] Y. Zhu, X. He, Y. Mo, Origin of Outstanding Stability in the Lithium Solid Electrolyte Materials: Insights from Thermodynamic Analyses Based on First-Principles Calculations, *ACS Appl. Mater. & Interfaces* 7 (42) (2015) 23685–23693, <http://dx.doi.org/10.1021/acsami.5b07517>, Publisher: American Chemical Society.
- [25] R. Murugan, V. Thangadurai, W. Weppner, Fast Lithium Ion Conduction in Garnet-Type Li₇La₃Zr₂O₁₂, *Angew. Chem. Int. Ed.* 46 (41) (2007) 7778–7781, <http://dx.doi.org/10.1002/anie.200701144>, eprint: <https://onlinelibrary.wiley.com/doi/pdf/10.1002/anie.200701144> URL <https://onlinelibrary.wiley.com/doi/abs/10.1002/anie.200701144>.
- [26] S. Boulineau, M. Courty, J.-M. Tarascon, V. Viallet, Mechanochemical synthesis of Li-argyrodite Li₆PS₅X (X=Cl, Br, I) as sulfur-based solid electrolytes for all solid state batteries application, *Solid State Ion.* 221 (2012) 1–5, <http://dx.doi.org/10.1016/j.ssi.2012.06.008>, URL <https://www.sciencedirect.com/science/article/pii/S0167273812003712>.
- [27] N. Kamaya, K. Homma, Y. Yamakawa, M. Hirayama, R. Kanno, M. Yonemura, T. Kamiyama, Y. Kato, S. Hama, K. Kawamoto, A. Mitsui, A lithium superionic conductor, *Nat. Mater.* 10 (9) (2011) 682–686, <http://dx.doi.org/10.1038/nmat3066>, Publisher: Nature Publishing Group URL <https://www.nature.com/articles/nmat3066>.
- [28] X. Li, J.T. Kim, J. Luo, C. Zhao, Y. Xu, T. Mei, R. Li, J. Liang, X. Sun, Structural regulation of halide superionic conductors for all-solid-state lithium batteries, *Nat. Commun.* 15 (1) (2024) 53, <http://dx.doi.org/10.1038/s41467-023-43886-9>, Publisher: Nature Publishing Group URL <https://www.nature.com/articles/s41467-023-43886-9>.
- [29] T. Dai, S. Wu, Y. Lu, Y. Yang, Y. Liu, C. Chang, X. Rong, R. Xiao, J. Zhao, Y. Liu, W. Wang, L. Chen, Y.-S. Hu, Inorganic glass electrolytes with polymer-like viscoelasticity, *Nat. Energy* 8 (11) (2023) 1221–1228, <http://dx.doi.org/10.1038/s41560-023-01356-y>, Publisher: Nature Publishing Group URL <https://www.nature.com/articles/s41560-023-01356-y>.
- [30] B. Ma, R. Li, H. Zhu, T. Zhou, L. Lv, H. Zhang, S. Zhang, L. Chen, J. Wang, X. Xiao, T. Deng, L. Chen, C. Wang, X. Fan, Stable Oxyhalide-Nitride Fast Ionic Conductors for All-Solid-State Li Metal Batteries, *Adv. Mater.* 36 (30) (2024) 2402324, <http://dx.doi.org/10.1002/adma.202402324>, eprint: <https://onlinelibrary.wiley.com/doi/pdf/10.1002/adma.202402324> URL <https://onlinelibrary.wiley.com/doi/abs/10.1002/adma.202402324>.